Parametric Study of Zigzag Microstructure for Vibrational Energy Harvesting

M. Amin Karami and Daniel J. Inman, *Fellow, ASME*

***Abstract*—A comprehensive parametric study is presented on the vibration and the energy harvesting performance of a low-frequency zigzag energy harvester. The zigzag microelectromechanical systems (MEMS) vibrational energy harvesters have low natural frequencies which match the low-frequency range of ambient vibrations. The harvesters can, therefore, be designed to resonate with ambient excitation. The power produced by energy harvesters at resonance is orders of magnitude larger than off resonance power. The paper aims at providing an easy-to-use, comprehensive tool for designing the harvesters for different applications. The two key characteristics of the vibrational energy harvesters are their resonance frequency and their power transfer function. We formulate both vibrations and power production of the zigzag MEMS harvesters in nondimensional equations. The paper advances the state of the art in MEMS energy harvesting research area by identifying the dimensionless parameters governing mechanical vibrations and energy generation. We also investigate how the resonant frequency and the maximum power vary with each of the corresponding dimensionless parameters. The graphs summarize the parametric studies and provide sufficient tools for design of zigzag harvesters. The natural frequencies are related to six dimensionless variables, and the power transfer functions depend on 12 dimensionless parameters. [2010-0298]**

***Index Terms*—Dimensionless, energy harvesting, low-frequency, microelectromechanical systems (MEMS), parametric study, piezoelectric.**

NOMENCLATURE

$\hat{a}_b = (d^2w_b/dt^2)/l\omega_1^2$	Dimensionless base acceleration.
BTR	Bending/torsion ratio.
b	the width of the lateral beams.
C_p	Total capacitance of the harvester.
$\widehat{C}_p = (\rho A l^3 \omega_1^2/\alpha^2)C_p$	Dimensionless capacitance
$c = \sqrt{\frac{YI}{\rho A}}$	
d	Distance between two adjacent beams.
$\widehat{d} = d/l$	Dimensionless distance between beams.
e_{31}	electric field-stress coupling coefficient in 31 direction (C/m^2) [1].
GJ	Torsional stiffness
$g = \sqrt{\frac{GJ}{I_p}}$	
h_p	Thickness of the piezoelectric layer.
h_s	Thickness of the substructure.
I_p	Polar mass moment of inertia.
j	The unit imaginary number, $\sqrt{-1}$.
$k = GJ/YI$	Stiffness parameter.
l	The length of each of the beams.
m_t	Tip mass.
$\widehat{m}_t = m_t/\rho Al$	Dimensionless tip mass.
m_l	Link mass.
$\widehat{m}_l = m_l/\rho Al$	Dimensionless link mass.
n	The total number of members.
P_t	State of the ith switch.
$\hat{p} = p/\rho Al\omega_1^3$	Dimensionless power.
R	The load resistance.
$\widehat{R} = \alpha^2 R/\rho A l^3 \omega_1$	Dimensionless load resistance.
V	Voltage across piezoelectric layer.
$\widehat{V} = (\alpha/\rho A l^3 \omega_1^2)V$	Dimensionless piezoelectric voltage.
$w_b(t)$	Base out-of-plane motion.
$w_i(x)$	Out-of-plane deformation of the ith beam.
$\widehat{w}_i = w_i/l$	Dimensionless out-of-plane deformation.
x	coordinate along each of the beams.
$\widehat{x} = x/l$	Dimensionless x-coordinate.
x_{end}	The x-coordinate of the free end.
x^*	The x-coordinate of the connection of two lateral beams.
Y_s	Young's modulus of substructure.
Y_p	Young's modulus of piezoelectric layer.
YI	Bending stiffness.
α	Electromechanical coupling coefficient.
$\beta_i(x)$	Twist angle of the ith beam.
γ	Torsional dimensionless parameter.
$\delta(x)$	Dirac delta function.
ϵ_{32}^s	Permittivity of the piezoelectric layer.
ζ	Damping ratio.
$\lambda_n = \omega_n l^2/c$	Dimensionless nth natural frequency.

Manuscript received October 15, 2010; revised April 28, 2011; accepted July 28, 2011. Date of publication November 22, 2011; date of current version February 3, 2012. This work was performed under the support of the U.S. Department of Commerce, National Institute of Standards and Technology, Technology Innovation Program, Cooperative Agreement Number 70NANB9H9007. This work was supported in part by the Institute for Critical Technology and Applied Science (ICTAS). Subject Editor N. Aluru.

The authors are with the Department of Aerospace Engineering, University of Michigan, Ann Arbor, MI 48109 USA (e-mail: karami@umich.edu; daninman@umich.edu).

Color versions of one or more of the figures in this paper are available online at http://ieeexplore.ieee.org.

Digital Object Identifier 10.1109/JMEMS.2011.2171321

$\widehat{\mu}_m$	Dimensionless forcing coefficient.
ρ_p	Density of the piezoelectric material.
ρ_s	Density of the substructure material.
ρA	Mass per unit length of the beams.
$\widehat{\psi}_m$	Dimensionless electromechanical coupling coefficient.
${}_i\phi_n$	nth bending mode shape of the ith member.
${}_i\widehat{\phi}_n = {}_i\phi_n/l$	Dimensionless bending mode shape.
$\widehat{\omega}_n = \omega_n/\omega_1$	Dimensionless natural frequency.

I. Introduction

VIBRATION ENERGY harvesters convert ambient vibrations to electrical energy. They can power small sensor nodes used for numerous applications where there is no easy access to a power grid. The alternative method of powering autonomous sensors has been using batteries. The batteries have to be changed frequently which can be troublesome particularly if the sensors are embedded or otherwise hard to get at. In addition, it is desired to make the power harvesters as small as possible. The microscale microelectromechanical system (MEMS) energy harvesters match the numerous commercially available MEMS sensors and can form ultra low weight, fully autonomous sensor nodes.

One of the main challenges facing development of MEMS energy harvesters is the frequency issue. The majority of vibrational energy harvesters are linear, which means they should be excited at resonance. This requires the natural frequency of the harvesters to be between 1 and 100 Hz, which has proven to be a major challenge, which we overcome in this paper. The early designs reported in the literature have the same thickness-to-length ratio as large-scale structures. This caused the corresponding natural frequencies to be in range of kHz [2]–[6]. In reality, to have a structure which is strong enough to sustain the vibrations, the thickness has to be proportional to its length squared. This means that the thickness-to-length ratio of MEMS structures has to be much less than that ratio of their large size counterparts. By choosing a thickness-to-length ratio of 1/100, Fang *et al.*[7] were able to achieve 600-Hz natural frequency. The trend was followed by [8]–[12] and natural frequencies of about 530, 460, 370, 325, and 100 Hz were achieved. The natural frequency has to be lowered further to match the ambient excitations, and the cantilever beam design is too simple to facilitate that. Yang *et al.*[13] presented a 7.5 mm by 7.5 mm rotary electrostatic power harvester with the first natural frequency at 110 Hz. In addition to the relatively large size of their harvester, their choice of spring geometry helped reduce the natural frequency.

The authors proposed using the zigzag design (Fig. 1) for MEMS vibrational energy harvesters [14]. They analytically studied and experimentally verified the natural frequencies and the mode shapes of the meandering structure and showed that a MEMS scale harvester with the useful natural frequency can be achieved by utilizing the zigzag design. It was shown that not only does a zigzag structure have a significantly lower natural frequency compared to a cantilever beam of the same dimensions, but also that the reduction of frequency is achieved without sacrificing the strength of the structure. The electromechanical vibrations of the harvester was also studied [15], and it was shown that using the zigzag design improves the power production of the MEMS harvesters by orders of magnitude.

Spiral structures [16], [17] have also been used to lower the natural frequency of the harvester. The main problem hindering the use of spiral geometry for harvesting application is the fact that the out-of-plane vibrations of the spirals are dominantly torsional [17]. This requires a complicated electrode configuration to be able to harness the generated energy.

The paper continues by a brief discussion of the zigzag structure and the governing equations for electromechanical vibrations. We then study the energy harvesting problem in two parts. The first part is the study of the vibrational characteristics of the device, i.e., its natural frequencies and mode shapes. For this part, we first perform a general dimensional analysis, which identifies the number of dimensionless parameters that describe the vibration problem. Nondimensionalizing the governing equations and the boundary, equilibrium, and continuity conditions reveals the dimensionless parameters. In the vibration analysis results section, we study the relation between each of the dimensionless parameters and the natural frequencies. Also, to better understand the power production, we distinguish the deflections due to the bending of the structure and the deformations due to torsion. Only bending of the harvester results in power generation, and we discuss which designs have larger bending deformations. We then move on to the second part which directly concerns power harvesting or in more technical terms, the forced electromechanical vibrations of the zigzag harvester. Similar to part one, we start with a general dimensional analysis and identify the number of dimensionless parameters that affect the power output. We then proceed by nondimensionalizing the forced vibration equation to find the dimensionless quantities. The first step in study of the forced response of the continuous vibration system is proving the orthogonality of the modes and mass normalizing each mode. We then derive the power production, voltage generation, and tip deformation frequency response functions. In the electromechanical results section, we study the variation of power output with each of the dimensionless parameters. The vibration and power production results not only reveal the relation between each of the design variables and the power output but also provide comprehensive easy-to-use tools for design and optimization of zigzag harvesters of all sizes and materials.

II. Zigzag Structure and the Governing Equations

The zigzag energy harvester is shown in Fig. 1(a). The base excitations make the structure vibrate in and out of the main plane. The structure is bilayered (Fig. 1(b)). The thin piezoelectric layer is typically few micrometers thick and is sandwiched between two ultra thin metal layers acting as electrodes. The base layer (or substructure) can be silicon and is normally much thicker than the piezoelectric layer. The structure is clamped at one end and supports a tip mass at its other end, forming a cantilever structure. This configuration is modeled as

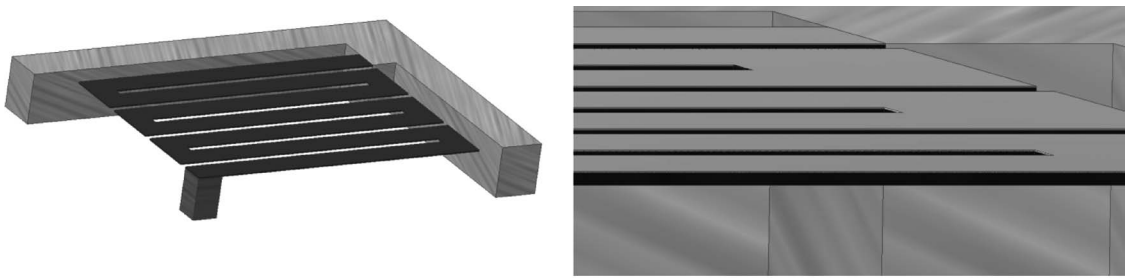

(a) (b)

Fig. 1. Zigzag structure. (a) The device. (b) The piezoelectric layer and the substrate.

a collection of straight beams, with rectangular cross sections, placed next to each other on the main plane. Each beam is connected to its neighbor beams at its ends by the link portions. Each of the beams can bend out of the main plane and can twist. Since the links are short, we model them as rigid connections. We do, however, take their mass into consideration. In fact, we consider the mass of the links as one of the design variables and study if we can increase power production by attaching large masses to the links.

When the structure bends, the charge generated by the piezoelectric material is collected by the electrodes, and the electrical energy is produced. Due to the electrode configuration, the torsion of the individual beams does not generate any voltage across the electrodes, and the harvested energy is attributed only to the bending in the structure.

Each of the individual members is a beam which can bend and twist. The mechanical vibration of the beam is excited by base oscillations and the electric voltage. The governing bending and torsional differential equations of each beam are [18], [19]

$$YI\frac{\partial^4 w_i}{\partial x^4}+\rho A\frac{\partial^2 w_i}{\partial t^2}=-\alpha\left[\frac{d\delta(x)}{dx}-\frac{d\delta(x-L)}{dx}\right]V(t)-[\rho A+m_l\delta(x-x^*)+m_t\delta(x-x_{\text{end}})]\ddot{w}_b(t) \quad (1)$$

$$GJ\frac{\partial^2\beta_i}{\partial x^2}-I_p\frac{\partial^2\beta_i}{\partial t^2}=0. \quad (2)$$

The coupling coefficient, α, is related to piezoelectric coupling by $\alpha=(e_{13}b/2)(h_p+(h_p^2-(Y_s/Y_p)h_s^2)/(h_p+(Y_s/Y_p)hs))$. The clamped condition at the base and the free condition at the tip result six essential and natural boundary conditions

$$w_1(0,t)=0,\frac{\partial w_1(0,t)}{\partial x}=0,\beta_1(0,t)=0 \quad (3)$$

$$\frac{\partial^2 w_n(x_{\text{end}},t)}{\partial x^2}=0,\frac{\partial^3 w_n(x_{\text{end}},t)}{\partial x^3}=\mp\frac{m_t}{EI}\omega^2 w_n(x_{\text{end}},t),\quad \frac{\partial\beta_n(x_{\text{end}},t)}{\partial x}=0. \quad (4)$$

In the above equations, x_{end} is the x-coordinate of the free end of the structure. If there are even number of beams in the meandering structure, x_{end} is 0, otherwise it is l. The vibrations of the individual beams are related to each other through continuity and equilibrium conditions [14]

$$\begin{aligned}W_t(x^*,t)&=d\times\beta_{i-1}(x^*,t)+w_{i-1}(x^*,t),\frac{\partial w_i(x^*,t)}{\partial x}\\&=\frac{\partial w_{i-1}(x^*,t)}{\partial x},\\ \beta_{i-1}(x^*)&=\beta_i(x^*)\end{aligned} \quad (5)$$

$$\begin{aligned}\frac{\partial^2 w_i(x^*,t)}{\partial x^3}&=\frac{-\partial^2 w_{i-1}(x^*,t)}{\partial x^2},YI\frac{\partial^3 w_{i-1}(x^*,t)}{\partial x^3}\\&=-YI\frac{\partial^3 w_i(x^*,t)}{\partial x^3}\mp m_l\ddot{w}_{i-1}(x^*,t),\end{aligned}$$

$$k\frac{\partial\beta_{i-1}(x^*,t)}{\partial x}=-k\frac{\partial\beta_i(x^*,t)}{\partial x}-\frac{\partial^3 w_i(x^*,t)}{\partial x^3}\times d. \quad (6)$$

The dimensionless parameter k is defined as $k=GJ/YI$ and x^* stands for the x-coordinate of the link between two adjacent members which can be either 0 or l.

In addition to the mechanical governing equations, the electrical equations should be considered. The members of the structure are electrically connected in parallel configuration as shown in Fig. 2. The switches shown in Fig. 2 (small boxes) can be used to reverse the polarity of the generated voltage (or current). They determine whether the voltage across each member is equal to the voltage across the load or is its negative. Correspondingly, the switches also identify weather the current going into each member should be added to or subtracted from the current in other members to give the total current passing through the load. The state of the ith switch is noted by P_i and is either 1 or -1. The current passing though each member is [20]

$$i_i(t)=-\alpha\frac{d}{dt\left(\int_0^l\frac{\partial^2 w_i}{\partial x^2}dx\right)-\frac{\epsilon_{33}^s blP_i}{h_p}\dot{\nu}(t)}. \quad (7)$$

The currents are added together, after being directed by the switches, and pass through the electrical load characterized by the resistance R. The voltage across the resistance which is the same in magnitude as the voltage across each beam is governed in part by the following equation:

$$C_p\dot{V}+\frac{V}{R}=-\alpha\sum_{i=1}^{n}P_i\frac{d}{dt}\left(\int_0^L\frac{\partial^2 W_i}{\partial x^2}dx\right). \quad (8)$$

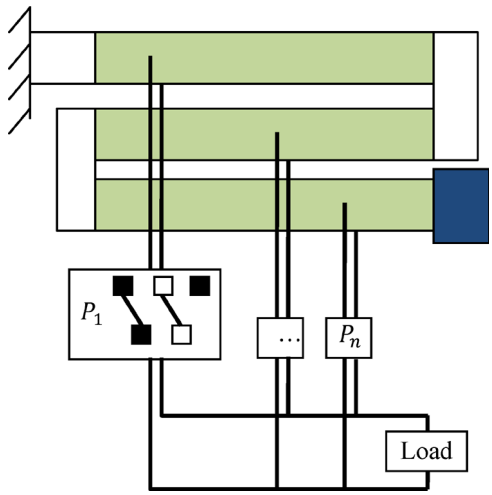

Fig. 2. Electrical connections, top view.

The total capacitance of the harvester, C_p, is

$$C_p = n\frac{\epsilon_{33}^s bl}{h_p}. \tag{9}$$

To use the modal analysis approach to solve this continuous vibration problem, we first find the natural frequencies and mode shapes of the mechanical structure. To this end, we consider the free vibrations equations

$$c^2\frac{\partial^4 w_t}{\partial x^4} + \frac{\partial^2 w_t}{\partial t^2} = 0, \quad c = \sqrt{\frac{YI}{\rho A}} \tag{10}$$

$$g^2\frac{\partial^2 \beta_i}{\partial x^2} = \frac{\partial^2 \beta_i}{\partial t^2}, \quad g = \sqrt{\frac{GJ}{I_p}}. \tag{11}$$

Seeking the nonzero solutions of (10) and (11) which satisfy the boundary, equilibrium, and continuity conditions (3)–(5) leads to finding the natural frequencies and mode shapes.

III. Dimensional Analysis

In this section, we look at the problem from a broad perspective and derive the number of dimensionless numbers that completely characterize the vibration problem. We specifically derive the dimensionless numbers later in Section IV. There are two key objectives in designing a vibrational energy harvester. The first is to tune the fundamental natural frequency to the frequency of ambient vibrations. The second goal is to maximize the harvested power. Accordingly, we first focus on the natural frequencies of the structure, and later we identify the number of dimensionless parameters that characterize the harvested power.

It can be seen from (5) and (6) and (10) and (11) that the natural frequencies of the zigzag structure are functions of the following parameters:

$$\omega_n = \omega_n\left(c, g, L, \frac{m_t}{EI}, \frac{m_l}{EI}, d, k, n\right). \tag{12}$$

The dimensions of the parameters are L^2T^{-1}, LT^{-1}, L, LT^2, LT^2, L,1, and 1 accordingly, and the dimension of the natural frequencies is T^{-1}. Since there are eight variables described by two dimensions, a dimensional analysis [21] suggests restatement of the physics as a relation between $9-2=7$ dimensionless variables. Here, instead of performing a pi-analysis to come up with the dimensionless parameters, we proceed by nondimensionalizing the governing equations and boundary conditions. The dimensionless variables will become evident during the analysis.

IV. Nondimensionalization of the Modal Analysis

Using separation of variables, (10) and (11) are converted into the following ordinary differential equations:

$$W_i^{(4)} - \frac{\omega_n^2}{c^2}W_i = 0, B_i'' + \left(\frac{\omega_n}{g}\right)^2 B_i = 0. \tag{13}$$

To put the above equations into the dimensionless form, the following dimensionless parameters are introduced:

$$\widehat{x} = \frac{x}{l}, \quad \widehat{w}_i = \frac{W_i}{l}. \tag{14}$$

Substituting for W from (14) in (13) and applying the chain rule result

$$\frac{d^4\widehat{w}_i(\widehat{x})}{d\widehat{x}^4} - \lambda^2\widehat{w}_i(\widehat{x}) = 0 \tag{15}$$

$$\frac{d^2 B_i(\widehat{x})}{d\widehat{x}^2} + \lambda^2\gamma^2 B_i(\widehat{x}) = 0. \tag{16}$$

In the above governing equations for bending and torsion of each member, the dimensionless parameters λ and γ are defined as

$$\lambda_n = \frac{\omega_n l^2}{c}, \quad \gamma = \frac{c}{gl} = \frac{\sqrt{\frac{YI}{\rho A}}}{l\sqrt{\frac{GJ}{I_p}}}. \tag{17}$$

So far, we have derived two of the seven dimensionless variables; λ_n is the dimensionless variable related to the nth natural frequency, and γ is the torsional dimensionless variable. The next two variables are derived by nondimensionalizing the tip mass natural boundary condition (4b) and the shear force equilibrium condition (6b)

$$\frac{d^3\widehat{w}_n(\widehat{x}_{\text{end}})}{d\widehat{x}^3} = \mp\,\widehat{m}_t\lambda^2\widehat{w}_n(\hat{x}_{\text{end}}) \tag{18}$$

$$\frac{\partial^3\widehat{w}_{i-1}(\widehat{x}^*)}{\partial\widehat{x}^3} = -\frac{\partial^3\widehat{w}_i(\widehat{x}^*)}{\partial\widehat{x}^3} \mp \widehat{m}_l\lambda^2\widehat{w}_{i-1}(\widehat{x}^*) \tag{19}$$

where the dimensionless variable $\widehat{m}_t$ is defined as $\widehat{m}_t = m_t/\rho Al$, and is the tip mass divided by the mass of a member. The link mass dimensionless variable, $\widehat{m}_l$, is similarly defined as $\widehat{m}_l = m_l/\rho Al$.

The last new dimensionless variable is revealed during nondimensionalization of the continuity condition. The following equation relates the displacement of two consecutive members at their point of connection (5a):

$$\widehat{w}_i(\widehat{x}^*) = \widehat{d}B_{i-1}(\widehat{x}^*) + \widehat{w}_{i-1}(\widehat{x}^*), \quad \widehat{d} = \frac{d}{l}. \tag{20}$$

The five introduced dimensionless parameters plus the dimensionless variables k and n form the seven dimensionless variables that fully describe the problem. The natural frequency dimensionless parameter can be expressed as a function of the rest of the dimensionless variables

$$\lambda_n = \lambda_n(n, \widehat{d}, \widehat{m}_t, \widehat{m}_l, k, \gamma). \tag{21}$$

To find the natural frequencies, we follow an approach similar to [14]. We consider the governing equations for the vibration of each of the members (15) and (16) and write the general solution in exponential form

$$\widehat{w}_i(\widehat{x}) = \sum_{j=1}^{4} A_{ij} e^{s_{ij}\widehat{x}},\ s_{ij} = \pm\sqrt{\lambda}, \pm i\sqrt{\lambda},\quad j = 1, 2, \ldots, 4 \tag{22}$$

$$B_i(\widehat{x}) = \sum_{j=5}^{6} A_{ij} e^{s_{ij}\widehat{x}},\ s_{ij} = \pm i\gamma\lambda. \tag{23}$$

The unknown coefficients A_{ij} are calculated by observing the boundary conditions at the clamped and free ends and also by preserving the equilibrium and continuity conditions at the connection points of consecutive members. Two of these condition have already been discussed in (18) and (20). The rest of these conditions are similar to those expressed in [14] and are not elaborated for brevity. Since all these $6 \times n$ conditions involve the coefficients A_{ij}, we can put all of them in a matrix relation

$$[\boldsymbol{M}]_{6n\times 6n}[A_{11}, \ldots, A_{16}, A_{21}, \ldots, A_{26}, \ldots, A_{n1}, A_{n6}]^T = \mathbf{0_{6n\times 1}}. \tag{24}$$

The determinant of the matrix $[M]$ depends on the exponents S_{ij} which in turn are functions of λ. The natural frequency parameters λ_n are those specific values which make the M-matrix singular and therefore allow nontrivial responses. To find the mode shapes corresponding to each natural frequency, the values of λ_n are substituted in (24), and the corresponding A_{ij} coefficients are derived. The mode shapes were previously plotted in [14].

V. Frequency Analysis Results

The natural frequency dimensionless parameters, λ_n, are functions of six dimensionless variables: n, $\widehat{d}$, $\widehat{m}_t$, $\widehat{m}_l$, k, and γ. The effects of individual dimensionless parameters on the frequency are discussed in this section. The illustrations have been arranged to make the results easy to use.

A. Relation Between the Natural Frequencies and the Number of Members

The natural frequencies significantly drop with the number of members. It can be inferred from Fig. 3 that the fundamental natural frequency of a 10-member structure is about 1/10 of the first natural frequency of a single cantilever beam. Also, the frequencies get more packed as the number of members increases. We discuss the implications of this fact for power harvesting in Section VIII-A.

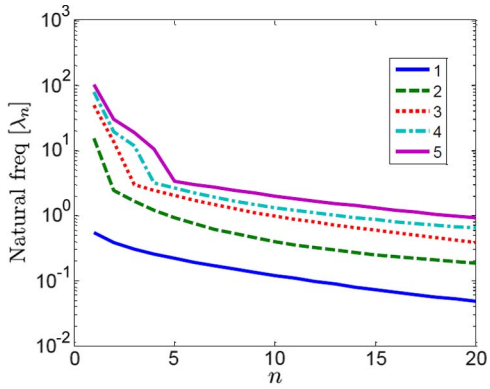

Fig. 3. Relation between the number of members and the first five natural frequencies; $\widehat{d} = 0.1$, $\widehat{m}_t = 10$, $\widehat{m}_l = 0$, $k = 1$, $\gamma = 0.02$; the legend shows the mode number.

B. Relation Between the Natural Frequencies and the Lateral Distance

Fig. 4 shows the relation between the first two natural frequencies and the dimensionless lateral distance between the consecutive beams. The natural frequencies drop as $\widehat{d}$ is increased. This suggests increasing the lateral distance to achieve lower natural frequency. Increasing the lateral distance, however, comes with a significant drawback, which is discussed in Section V-G.

C. Relationship Between the Natural Frequencies and the Stiffness Ratio

The dimensionless parameter k indicates the torsion/bending stiffness ratio. An increase in this ratio means an increase in torsional stiffness while the bending stiffness is constant. This results in the direct relationship between the first two natural frequencies and the stiffness ratio which is shown in Fig. 5.

D. Relationship Between the Natural Frequencies and γ

The dimensionless analysis shows that the torsional parameter γ has a negligible influence on the natural frequencies. Therefore, with a very good approximation, we can remove the parameter γ from our vibration study and reduce the dimension of the problem by one.

E. Relationship Between the Natural Frequencies and the Tip Mass

Generally, adding tip mass reduces all of the resonant frequencies. Fig. 6 shows that if the dimensionless tip mass is less than 1, the tip mass effects are small. The fundamental mode is the most sensitive mode to the tip mass. If the normalized tip mass is larger than one, i.e., the tip mass is more than the mass of a single beam, the fundamental natural frequency is inversely proportional to $\sqrt{\widehat{m}_h}$. Fig. 6(b)–(d) shows that the second mode is not as sensitive to variations of the tip mass.

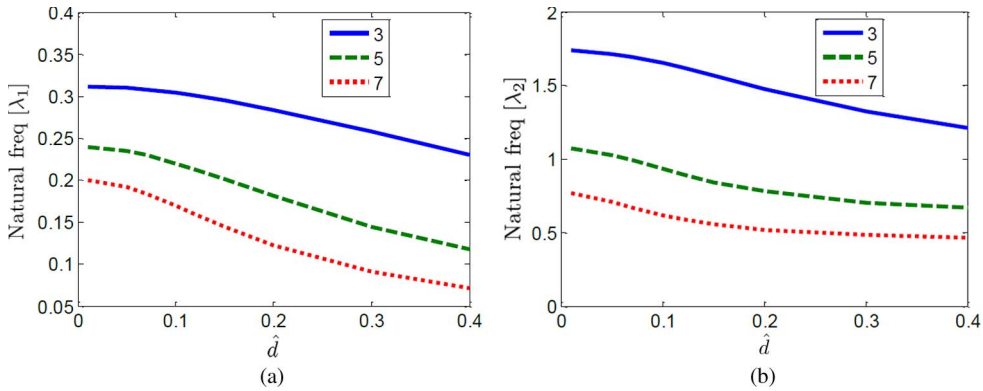

Fig. 4. Relation between $\widehat{d}$ and the first four natural frequencies: (a) mode 1, (b) mode 2, $\widehat{m}_t = 10$, $\widehat{m}_l = 0$, $k = 1$, $\gamma = 0.02$, the legend shows the number of beams.

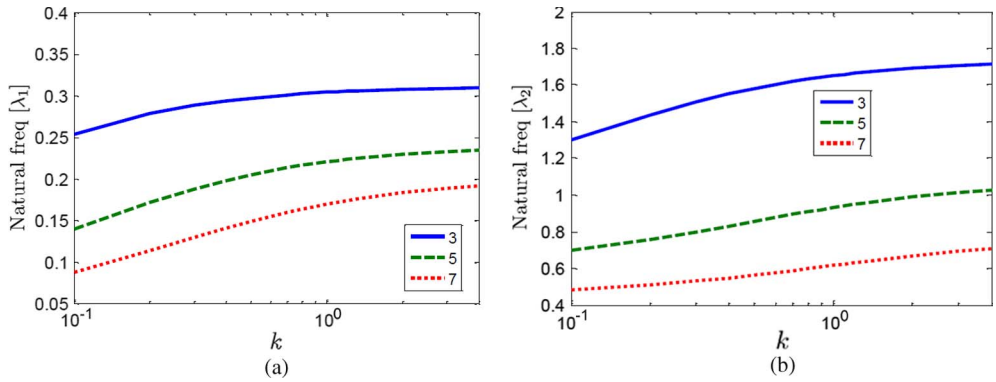

Fig. 5. Relation between k and the natural frequencies: (a) mode 1, (b) mode 2, $\widehat{d} = 0.1$, $\widehat{m}_t = 10$, $\widehat{m}_l = 0$, $\gamma = 0.02$, the legend shows the number of beams.

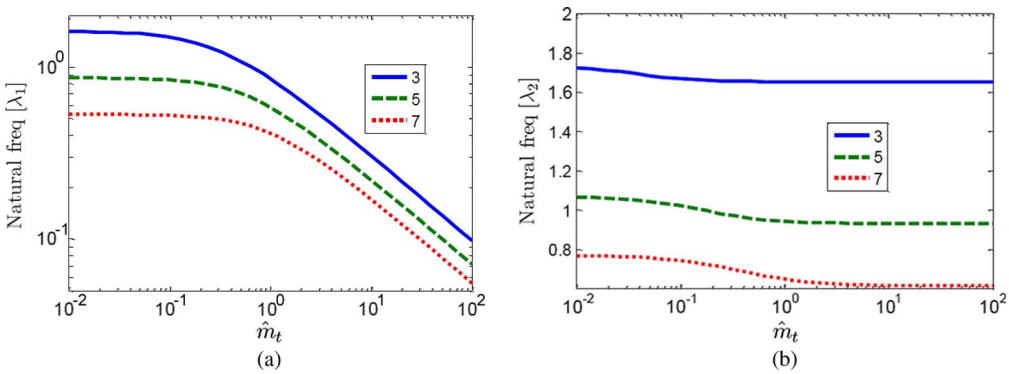

Fig. 6. Effect of $\widehat{m}_t$ on natural frequencies: (a) mode 1,(b) mode 2, $\widehat{d} = 0.1$, $\widehat{m}_l = 0$, $k = 1$, $\gamma = 0.02$, the legend shows the number of beams.

F. Relationship Between the Natural Frequencies and the Link Mass

Similar to the tip mass, the link masses reduce the natural frequencies of the structure. It has been assumed that all the links in the zigzag structure have the same mass. It is possible to place large link masses to reduce the natural frequency of the structure. As Fig. 7 shows, the tip masses reduce the resonant frequency of the higher modes as well as the fundamental. The link mass effect on first natural frequency becomes prominent when the dimensionless link mass, i.e., the link mass divided by the mass of a single beam, is larger than both 1 and the normalized tip mass. In that case, the fundamental frequency is inversely proportional to the square root of the dimensionless link mass.

G. Contribution of Bending Deformation

The coupling coefficients for harvesting from torsional and bending deflections are different. As shown in Fig. 8, this causes the direction of the electric field to be different in

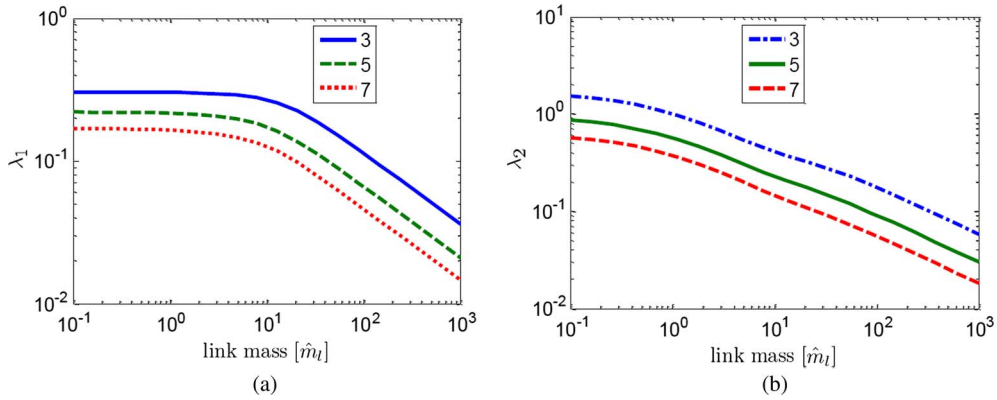

Fig. 7. Effect of $\widehat{m}_l$ on natural frequencies: (a) mode 1, (b) mode 2, $\widehat{d} = 0.1$, $\widehat{m}_t = 10$, $k = 1$, $\gamma = 0.02$, the legend shows the number of beams.

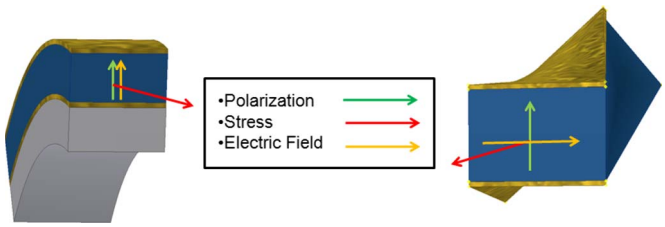

Fig. 8. Electric field directions in bending and torsional deformation.

bending and torsional deformation. Since there is only one pair of electrodes placed at the top and bottom surfaces of the piezoelectric layer, energy can only be harvested from the bending vibrations of the piezoelectric structure. The bending index is defined as the ratio between the bending potential energy over the overall elastic potential energy, as shown by the equation at the bottom of the page.

If the mode shapes indicate that the deflection is solely due to bending of the members (for example, the mode shapes of a single beam), the value of bending/torsion ratio (BTR) is one. In contrast, if the deflections are dominantly torsional (deflection of a zigzag structure with too many members), BTR equals zero. Fig. 9 shows that the first mode becomes more torsional as the number of members increases. Although the BTR for the even modes varies as the number of members changes, the vibration of these modes is always dominantly in bending. We are mostly interested in energy harvesting from the fundamental mode since it corresponds to the lowest natural frequency. Fig. 9 also shows that the tip mass can be utilized to improve the bending deformation of the first mode. The lateral distance between the members (characterized by $\widehat{d}$) also affects the available bending energy in the structure. As shown in Fig. 10, the lateral distance has a prominent effect on the BTR. The less the distance, the more bending occurs in the fundamental mode of the structure. This suggests using narrow members in the structure to reduce the distance between the centerlines.

VI. Dimensional Analysis of the Electromechanical Problem

We are interested in finding the transfer function between the base vibrations, w_b, and the output voltage, V, and the electric power in the frequency domain as this is also important in design. Considering the damping in the structure, the frequency response function is a function of the excitation frequency and the design variables

$$\frac{V(\omega)}{W_b(\omega)} = f(\omega, \zeta, C_p, R, \rho A, l, \alpha, \text{modal parameters}).$$

The modal parameters refer to the natural frequencies and the mode shapes, which as discussed in Section IV are in turn functions of n, $\hat{d}$, $\hat{m}_t$, $\hat{m}_l$, k, and γ. The harvested power is therefore function of these parameters

$$p = p(W_b, \omega, \zeta, C_p, R, \rho A, c, \alpha, l, P_i, n, \hat{d}, \widehat{m}_t, \widehat{m}_l, k, \gamma). \tag{25}$$

The dimensions of the parameters in (25) are, L, T^{-1}, 1, $Q^2T^2M^{-1}L^{-2}$, $ML^2Q^{-2}T^{-1}$, ML^{-1}, L^2T^{-1}, Q, L, 1, 1, 1, 1, 1, and 1. The dimension of the power is ML^2T^{-3}. There are 17 interrelated parameters and four dimensions. Therefore, $17 - 4 = 13$ dimensionless parameters are required to describe the relation. So far, we have identified eight of the dimensionless parameters (n, $\widehat{d}$, $\widehat{m}_t$, $\widehat{m}_l$, k, γ, P_i, and ζ). The remaining five will be derived in the next section.

VII. Nondimensionalization of the Electromechanical Formulation

This section considers the forced electrometrical vibrations of the structure described by (1) and (2) and (8). We first consider the mechanical side of the governing equations. (1) and (2) are written in terms of modal coordinates, are premultiplied by the mode shapes, and are integrated all over the structure.

$$BTR = \frac{\frac{1}{2}\int_{\text{all members}} YI\left(\widehat{w}''(\widehat{x})\right)^2 d\widehat{x}}{\frac{1}{2}\int_{\text{all members}} YI\left(\widehat{w}''(\widehat{x})\right)^2 dy + \frac{1}{2}\int_{\text{all members}} GJ\left(B'(\hat{x})\right)^2 d\hat{x}}$$

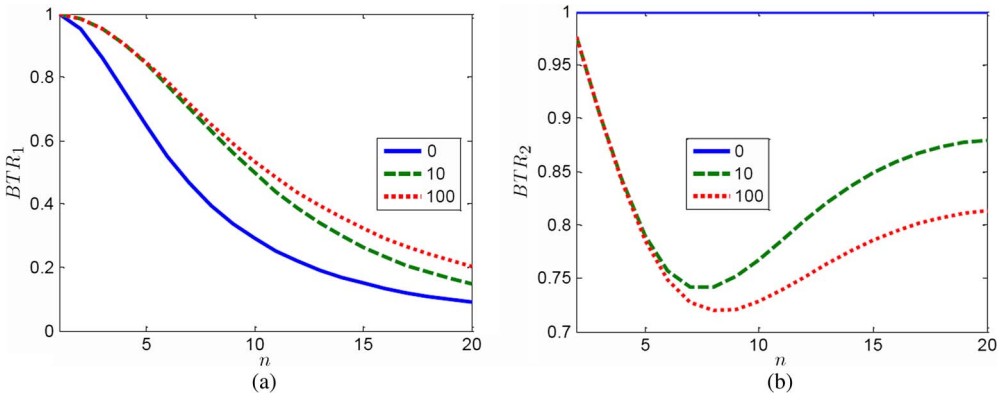

Fig. 9. Effect of the number of beams on bending/torsion ratio: (a) mode 1, (b) mode 2, $\widehat{m}_l = 0$, $k = 1$, $\gamma = 0.02$, the legend shows $\widehat{m}_t$.

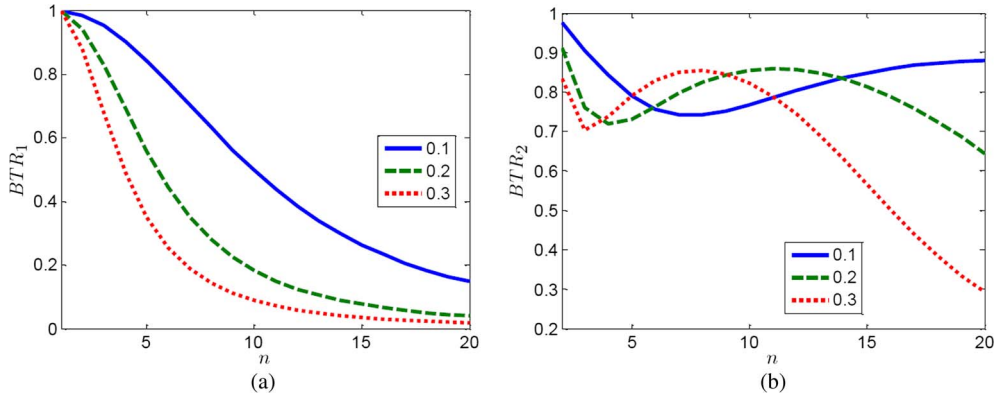

Fig. 10. Effect of the number of beams on bending/torsion ratio: (a) mode 1, (b) mode 2, $\widehat{m}_t = 10$, $\widehat{m}_l = 0$, $k = 1$, $\gamma = 0.02$, the legend shows $\widehat{d}$.

Applying the orthogonality conditions [refer to Appendix, (45) and (46)] results in

$$\sum_{i=1}^{n}\left[YI\int_0^L ({}_i\phi_m'')^2\,dx + GJ\int_0^L ({}_iB_m')^2\,dx\right]T_m(t) + \left\{\sum_{i=1}^{n}\left[\rho A\int_0^L ({}_i\phi_m)^2dx + I_p\int_0^L ({}_iB_m)^2dx\right] + m_t\,({}_n\phi_m(x_{\text{end}}))^2 + \sum_{i=1}^{n-1} m_l\,({}_i\phi_m(x^*))^2\right\}\ddot{T}_m(t) = -\alpha V(t)\sum_{i=1}^{n} p_i\,[{}_i\phi_i'(L) - {}_i\,\phi_i'(O)] - \ddot{w}_b(t) \times\left[\sum_{i=1}^{n}\rho A\int_0^L {}_i\phi_n(x)dx + \sum_{i=1}^{n-1} m_l\,{}_i\phi_m(x^*) + m_t\,{}_n\phi_m(x_{\text{end}})\right]. \tag{26}$$

We then introduce the following change of variables to nondimensionalize the equations:

$${}_i\widehat{\phi}_m = \frac{{}_i\phi_m}{l},\quad \widehat{x} = \frac{x}{l},\quad k = \frac{GJ}{YI},\quad \lambda_m = \omega_m l^2\sqrt{\frac{\rho A}{YI}},$$
$$\widehat{V} = \frac{\alpha}{\rho A l^3\omega_1^2}V,\quad \widehat{m}_t = \frac{m_t}{\rho A l},\quad \widehat{m}_l = \frac{m_l}{\rho A l},$$
$$\hat{I}_p = \frac{I_p}{\rho A l^2} = \frac{\gamma^2}{k}$$
$$\widehat{\omega}_n = \frac{\omega_n}{\omega_1},\quad \tau = \omega_1 t,\quad \widehat{w}_b = \frac{w_b}{l}. \tag{27}$$

The change of variables in (27) puts (26) in the corresponding dimensionless form below

$$\sum_{i=1}^{n}\left[\int_0^1\left(\frac{d^2\,{}_i\hat{\phi}_m}{d\hat{x}^2}\right)^2 d\hat{x} + k\int_0^1\left(\frac{d_i B_m}{d\hat{x}}\right)^2 d\hat{x}\right]T_m(\tau) + \lambda_1^2\left\{\sum_{i=1}^{n}\left[\int_0^1 {}_i\hat{\phi}_m^2 d\hat{x} + \hat{I}_p\int_0^1 ({}_iB_m)^2 d\hat{x}\right] + \hat{m}_l\,{}_n\hat{\phi}_m^2(\hat{x}_{\text{end}}) + \sum_{i=1}^{n-1} m_t\,{}_i\hat{\phi}_m^2(\hat{x}^*)\right\}\frac{d^2T_m(\tau)}{d\tau^2} = -\lambda_1^2\hat{V}(\tau)\sum_{i=1}^{n} p_i\left[\frac{d_i\hat{\phi}_m(1)}{d\hat{x}} - \frac{d_i\hat{\phi}_m(0)}{d\hat{x}}\right] - \lambda_1^2\frac{d^2\hat{w}_b}{d\tau^2} \times\left[\sum_{i=1}^{n}\int_0^1 {}_i\hat{\phi}_m(\hat{x})d\hat{x} + \sum_{i=1}^{n=1}\hat{m}_l\,{}_i\hat{\phi}_m(\hat{x}^*) + \hat{m}_t\,{}_n\hat{\phi}_m(\hat{x}_{\text{end}})\right]. \tag{28}$$

If we mass normalize the already dimensionless mode shapes according to the following equation:

$$\sum_{i=1}^{n}\left[\int_0^1 {}_i\widehat{\phi}_m^2 d\widehat{x} + \hat{I}_p\int_0^1 ({}_iB_m)^2 d\widehat{x}\right] + \widehat{m}_t\,{}_n\widehat{\phi}_m^2(\widehat{x}_{\text{end}}) + \sum_{i=1}^{n-1}\widehat{m}_l\,{}_i\widehat{\phi}_m^2(\hat{x}^*) = 1. \quad (29)$$

From (46) and (28), we have the following final dimensionless form of the mechanical governing equation:

$$\frac{d^2T_m(\tau)}{d\tau^2} + T_m(\tau) = -\widehat{\psi}_m\widehat{V}(\tau) - \widehat{\mu}_m\frac{d^2\widehat{w}_b}{d\tau^2} \quad (30)$$

where the dimensionless electromechanical coupling coefficient, $\widehat{\psi}_m$, and the dimensionless forcing coefficient, $\widehat{\mu}_m$, are defined as

$$\widehat{\psi}_m = \sum_{i=1}^{n} P_i\left[\frac{d_i\widehat{\phi}_m(1)}{d\widehat{x}} - \frac{d_i\widehat{\phi}_m(0)}{d\widehat{x}}\right] \quad (31)$$

$$\widehat{\mu}_m = \sum_{i=1}^{n}\int_0^1 {}_i\widehat{\phi}_m(\widehat{x})d\widehat{x} + \sum_{i=1}^{n-1}\widehat{m}_l\,{}_i\widehat{\phi}_m(\widehat{x}^*) + \widehat{m}_t\,{}_n\widehat{\phi}_m(\widehat{x}_{\text{end}}). \quad (32)$$

Equation (30) manifests the mechanical vibrations which are influenced by the base excitation and are interrelated to the electric voltage. We define dimensionless base acceleration as $\hat{a}_b = d^2\widehat{w}_b/d\tau^2$. It is interesting to see that $\hat{a}_b = (d^2w_b/dt^2)/l\omega_1^2$.

On the electrical side, the current generated due to the piezoelectric effect passes through the resistive load and the capacitor made by the two electrodes on the surfaces of the piezoelectric layer. Using the same dimensionless parameters in (27), we can nondimensionalize (8) to

$$\widehat{C}_p\frac{d\widehat{V}}{dt} + \frac{\widehat{V}}{\widehat{R}} = \sum_{m=1}^{\infty}\widehat{\psi}_m\frac{dT_{m(\tau)}}{d\tau} \quad (33)$$

where $\widehat{\psi}_m$ has been defined before, and dimensionless capacitance and resistance are defined as

$$\widehat{C}_p = \frac{\rho AL^3\omega_1^2}{\alpha^2}C_p \quad \widehat{R} = \frac{\alpha^2 R}{\rho AL^3\omega_1}. \quad (34)$$

Taking the key mechanical equation, (30), and the key electrical equation, (33), to Fourier domain, we get the following transfer function between the voltage across the load and the base excitation:

$$\frac{\widehat{V}(\widehat{\omega})}{\hat{a}_b(\widehat{w})} = -\frac{\sum_{m=0}^{\infty}\frac{\widehat{\mu}_m\widehat{\psi}_m}{\widehat{\omega}_m^2+2\zeta\widehat{\omega}\widehat{\omega}_m-\widehat{\omega}^2}}{\frac{1}{\widehat{R}j\widehat{\omega}} + \widehat{C}_p + \sum_{m=0}^{\infty}\frac{\widehat{\psi}_m^2}{\widehat{\omega}_m^2+2\zeta\widehat{\omega}\widehat{\omega}_m-\widehat{\omega}^2}} \quad (35)$$

where $\widehat{\omega}$ is the dimensionless natural frequency and is defined as $\widehat{\omega} = \omega/\omega_1$. Although we cannot express the power as a frequency response function, the following fraction gives the power output when the base excitation is composed of only one frequency:

$$\frac{\widehat{p}(\widehat{\omega})}{\widehat{a}_b^2(\widehat{\omega})} = \frac{1}{2\widehat{R}}\left(\frac{\sum_{m=0}^{\infty}\frac{\widehat{\mu}_m\widehat{\psi}_m}{\widehat{\omega}_m^2+2\zeta\widehat{\omega}\widehat{\omega}_m-\widehat{\omega}^2}}{\frac{1}{\widehat{R}j\widehat{\omega}} + \widehat{C}_p + \sum_{m=0}^{\infty}\frac{\widehat{\psi}_m^2}{\widehat{\omega}_m^2+2\zeta\widehat{\omega}\widehat{\omega}_m-\widehat{\omega}^2}}\right). \quad (36)$$

At this point, we have successfully put the power production problem as an exact relation among 13 dimensionless numbers. The additional five dimensionless numbers that we predicted in Section VI are: $\hat{p}$, $\hat{\omega}$, $\hat{a}_b$, $\widehat{R}$, and $\widehat{C}_p$. Note that the modal parameters, $\widehat{\mu}_m, \widehat{\psi}_m, \widehat{\omega}_m$ are all in turn functions of n, $\hat{d}$, $\hat{m}_t$, $\hat{m}_l$, k, and γ. The actual and dimensionless power are related as

$$p = \hat{p}\rho Al^3\omega_1^3. \quad (37)$$

The Fourier transform of the temporal function $T_m(\tau)$ is noted by $T_m(\omega)$ and is calculated from (30) and (35) as (38),shown at the bottom of the next page.

The tip deflection can then be calculated by summing the effect of individual modes

$$\frac{\widehat{w}_t(\widehat{\omega})}{\hat{a}_b(\widehat{\omega})} = \sum_{m=1}^{\infty}\frac{T_m(\widehat{\omega})}{\hat{a}_b(\widehat{\omega})}\,{}_n\widehat{\phi}_m(x_{\text{end}}). \quad (39)$$

VIII. Electromechanical Power Production Results

The dimensionless power is a function of n, $\hat{d}$, $\hat{m}_t$, $\hat{m}_l$, k, γ, P_i, ζ, $\widehat{\omega}$, $\hat{a}_b$, $\widehat{R}$, and $\widehat{C}_p$. In this section, we present the relation between each of the parameters and the power production. The polarity of the switches is always optimized based on the fundamental mode according to the scheme presented in [15]. The typical values of dimensionless parameters for MEMS harvesters are: $\widehat{d} = 0.1$, $\widehat{m}_t = 100$, $\widehat{m}_l = 0.1$, $k = 1$, $\gamma = 0.01$, $\widehat{C}_p = 10$, and $\zeta = 0.01$. To examine the effect of each dimensionless variable, we change only that parameter and keep the others fixed at the values specified above. In each study, we consider a few structures with different number of beams, n.

A. Excitation Frequency and Load Resistance

The power outputs of all linear vibrational energy harvesters are sensitive to the excitation frequency and the load resistance. This is also the case with zigzag microharvesters. Fig. 11 shows the dimensionless power output of 1-, 3-, 7-, and 12-member structures as a function of the excitation frequency. The powers peak at resonance frequencies. The best excitation frequency is the fundamental natural frequency. There are two reasons for the superiority of the fundamental mode. First, the switches have been set according to the first mode shape. This selection minimizes power cancelation of the first mode but is not optimal for the higher modes. The second reason is that the parameters μ_i and ψ_i corresponding to higher modes are much less than those of the first mode. This means that

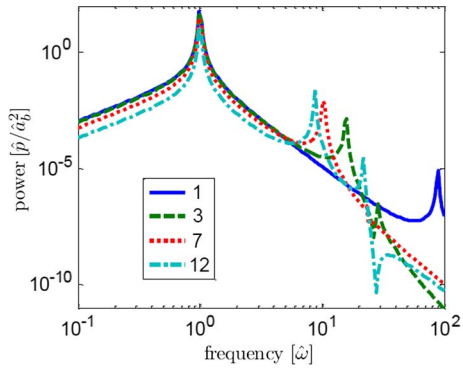

Fig. 11. Power output frequency response function; the legend shows the number of beams.

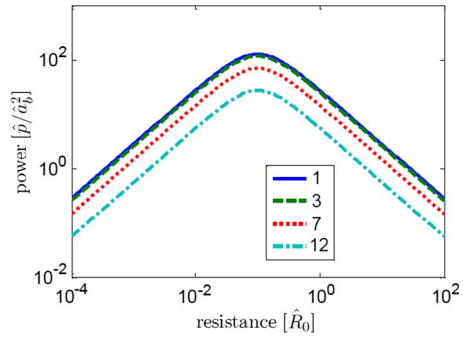

Fig. 12. Relation between the power output transfer function at $\widehat{\omega} = 1$ and the load resistance; the legend shows the number of beams.

the higher modes are less excited and also have less charge generation compared to the fundamental mode. This causes the optimal power to correspond to $\widehat{\omega} = 1$. Note that since the fundamental frequencies of structures with different number of members are different, the $\widehat{\omega} = 1$ translates to different physical frequencies depending on n. We can also observe from Fig. 11 that the more members the structure has, the closer the first two natural frequencies become. This implies that the zigzag structures with a large number of members are more beneficial for broadband energy harvesting.

There is also an optimal value for the load resistance. Fig. 12 shows that the power increases proportional to $\widehat{R}$ until it peaks at the optimal resistance and then decreases inversely proportional to $\widehat{R}$. The optimal load is not the same for different number of members. From this point on, we focus on the power output when the excitation frequency and the load resistance are at their optimal values. This is a reasonable approach since we can tune the natural frequency using the analysis in Section V, and we can also use a Buck Boost transformer [22], [23] to match the optimal resistive load.

B. Capacitance of the Piezoelectric Layer

Another parameter that affects the dimensionless power output is the dimensionless capacitance, $\widehat{C}_p$. As mentioned before, the output power discussed is the optimal power meaning that the excitation frequency and resistive load are at their optimal values. The optimal excitation frequency is always very close to $\widehat{\omega} = 1$. The optimal resistance however varies case by case, and we therefore plot that in addition. Fig. 13(a) shows that only after a certain threshold does $\widehat{C}_p$ have visible effects on power production. Beyond this threshold, which depends on the number of members, the power is inversely proportional to the capacitance. If the capacitance of the piezoelectric layer is larger than the threshold, the optimal resistance shown in Fig. 13(b) would solely depend on $\widehat{C}_p$. In that region, the optimal resistance is inversely proportional to the dimensionless capacitance. Typically, the $\widehat{C}_p$ is larger than 1 which implies that the capacitance does affect the power output and the dimensionless optimal resistance does not directly depend on the number of beams.

C. Damping Ratio

Generally, a smaller damping ratio corresponds to more power production, but the sensitivity of the power to damping ratio varies. Here, again we consider the power production when both the excitation frequency and load resistance are optimal. If the damping ratio is larger than a certain value, the mechanical vibrations of the device are not affected by the harvested energy. In this range, the power is inversely proportional to the damping ratio square. Fig. 14(a) shows that the value of the critical damping ratio depends on the number of members and that the larger structures have less critical damping. If the structural damping is less than the critical value, the energy dissipation in the mechanical system is mainly the harvested energy. In this range, the power is still related to damping ratio and is inversely proportional to ζ. The optimal resistance is insensitive to damping ratio if ζ is larger than the critical damping as suggested by Fig. 14(b).

D. Tip Mass

The harvested power increases with the tip mass. However, the relation between the power and tip mass is more complicated than the dependence of natural frequencies on the tip mass [Fig. 15(a)]. The optimal resistance in structures with only a few members significantly increases with the increase of tip mass, but for structures with more than 12 members, the optimal resistance is indifferent to the dimensionless tip mass.

$$\frac{T_n(\widehat{\omega})}{\hat{a}_b(\widehat{\omega})} = -\frac{1}{\widehat{\omega}_n^2 + 2\zeta\widehat{\omega}\widehat{\omega}_n - \widehat{\omega}^2}\left(\widehat{\mu}_n - \widehat{\psi}_n \frac{\sum_{m=0}^{\infty} \frac{\widehat{\mu}_m \widehat{\psi}_m}{\widehat{\omega}_m^2 + 2\zeta\widehat{\omega}\widehat{\omega}_m - \widehat{\omega}^2}}{\frac{1}{\widehat{R}j\widehat{\omega}} + \widehat{C}_p + \sum_{m=0}^{\infty} \frac{\widehat{\psi}_m^2}{\widehat{\omega}_m^2 + 2\zeta\widehat{\omega}\widehat{\omega}_m - \widehat{\omega}^2}}\right) \tag{38}$$

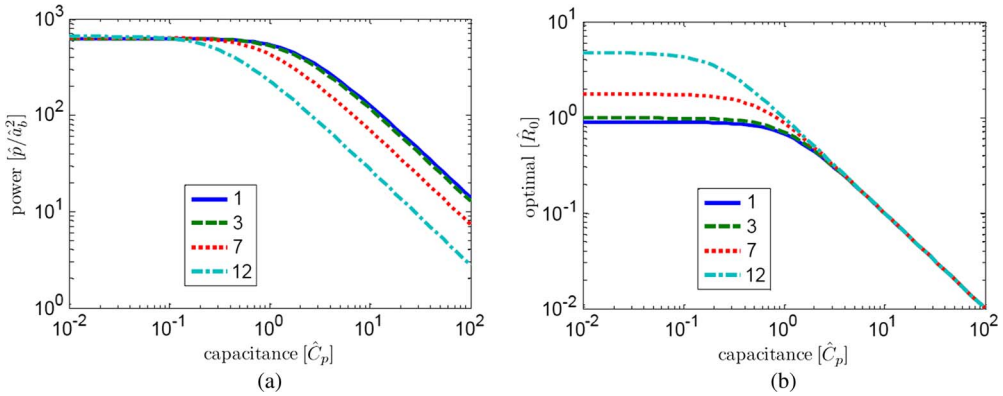

Fig. 13. Effect of the capacitance on (a) the maximum power transfer function and (b) the optimal resistance; the legend shows the number of beams.

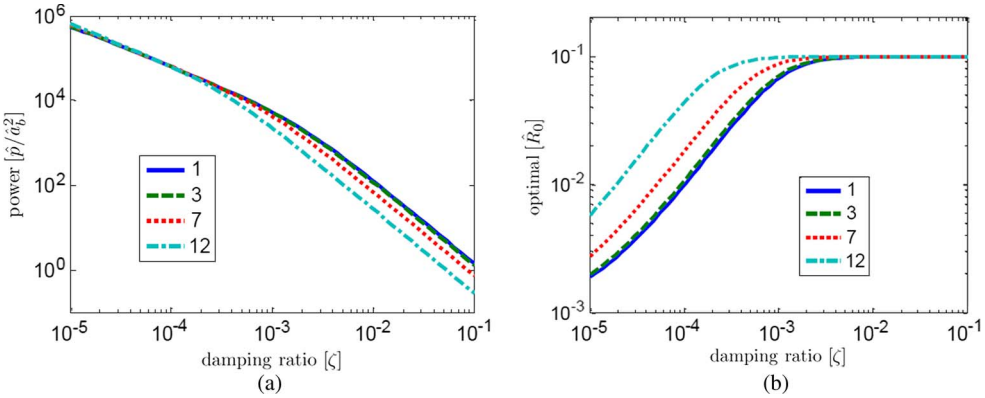

Fig. 14. Effect of the damping ratio on (a) the maximum power transfer function and (b) the optimal resistance; the legend shows the number of beams.

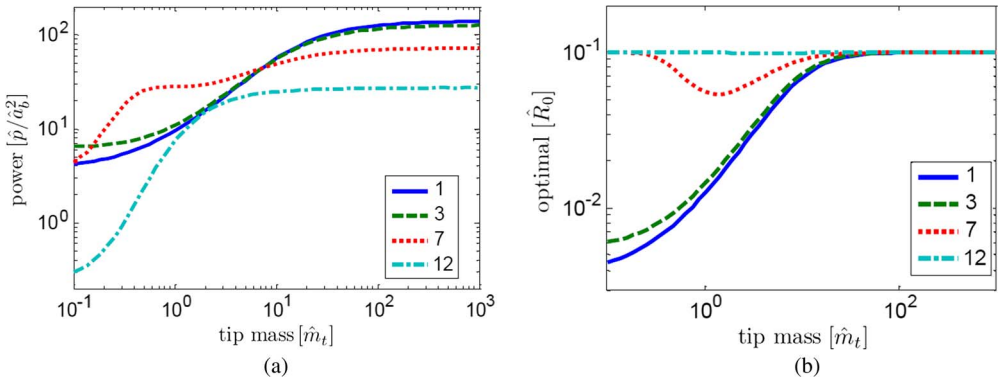

Fig. 15. Effect of the tip mass on (a) the maximum power transfer function and (b) the optimal resistance; the legend shows the number of beams.

E. Link Mass

Interestingly, increasing the link masses does not necessarily increase the power output. In fact, there is a crucial link mass [Fig. 16(a)] which significantly deteriorates the power production. As the link masses increase, the vibrations of each of the beams resemble vibrations of clamped-clamped beams. In this situation, the charge cancelation becomes significant and the power decreases. The antiresonance in power corresponds to perfect power cancellation in each of the beams. The optimal resistance is almost insensitive to the link masses [Fig. 16(b)].

F. Torsional Dimensionless Variable

The dimensionless electromechanical analysis indicated that the torsional dimensionless variable γ has no effect on the power output. The optimal load is also unrelated to γ. Section V-D discussed that the parameter γ has a negligible effect on the natural frequency. We, therefore, with a good approximation can neglect the torsional dimensionless variable, γ, in both frequency and power analyses.

G. Lateral Distance of the Beams

It is shown in Fig. 17(a) that the power output severely drops if the lateral distance between the members is larger than a critical value. The critical value depends on the number of members forming the structure. The power drop is associated with the bending to torsion ratio discussed in Section V-G. Increasing the lateral distance reduces the fundamental natural frequency but at the same time increases the torsion in the

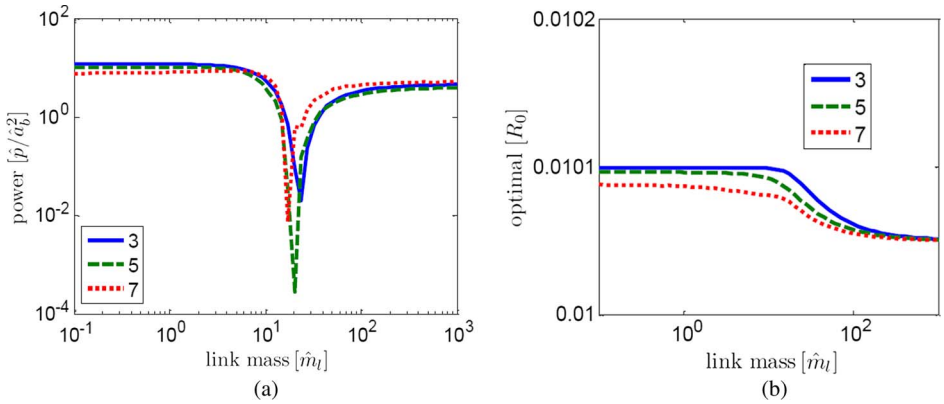

Fig. 16. Effect of the link mass on (a) the maximum power transfer function and (b) the optimal resistance; the legend shows the number of beams.

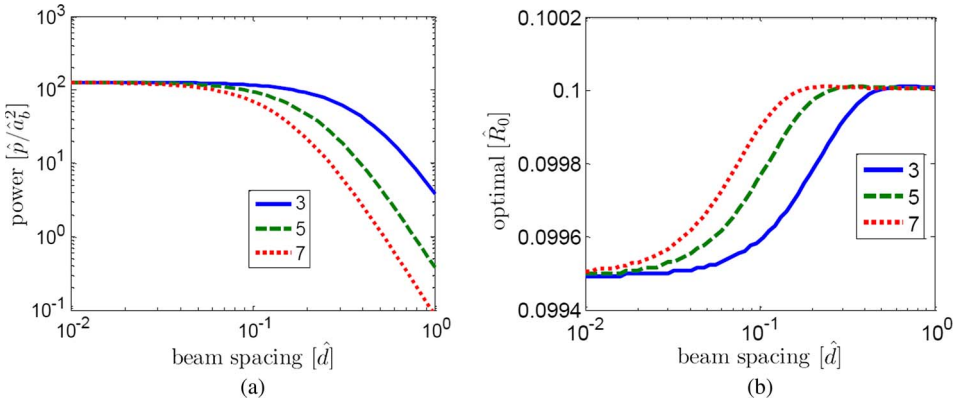

Fig. 17. Effect of the lateral distance on (a) the maximum power transfer function and (b) the optimal resistance; the legend shows the number of beams.

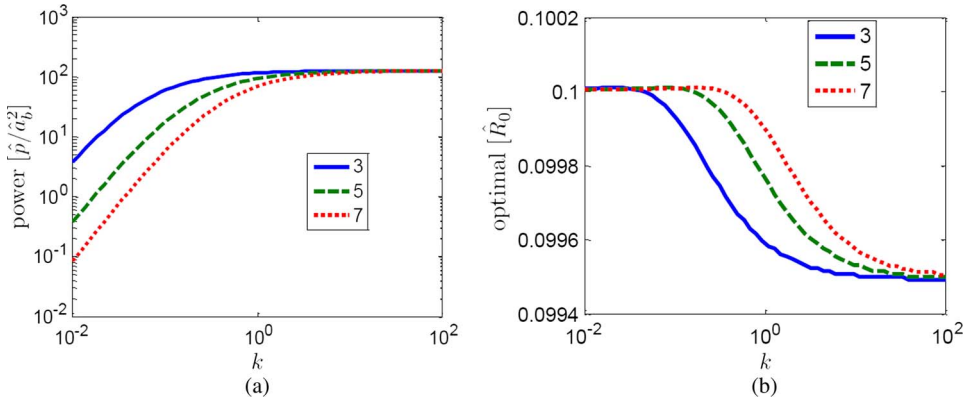

Fig. 18. Effect torsion/bending stiffness ratio on (a) the maximum power transfer function and (b) the optimal resistance; the legend shows the number of beams.

structure. As the vibrations become torsional, the harvested power drops. The optimal resistance is almost insensitive to lateral distance as shown in Fig. 17(b).

H. Torsion/Bending Stiffness Ratio

The amount of bending deformation discussed in Section V-G explains the direct relation between the power output and the stiffness ratio parameter, k. The larger the stiffness ratio, the more torsional stiffness and the larger the share of bending in total deformation. Therefore, below a critical value of k, which depends on the number of members, the power is proportional to the second power of torsion/bending stiffness ratio (Fig. 18). The optimal resistance is almost insensitive to the stiffness ratio.

I. Number of Members

Thus far, the parameter study was performed by fixing all except one of the dimensionless parameters and observing the power and optimal dimensionless resistance variations. The approach is altered for studying the role of the number of members, since change of the number of members intrinsically changes the capacitance, natural frequencies, and other dimensionless parameters. In the case, our approach is based on considering a MEMS harvesting device and plotting the

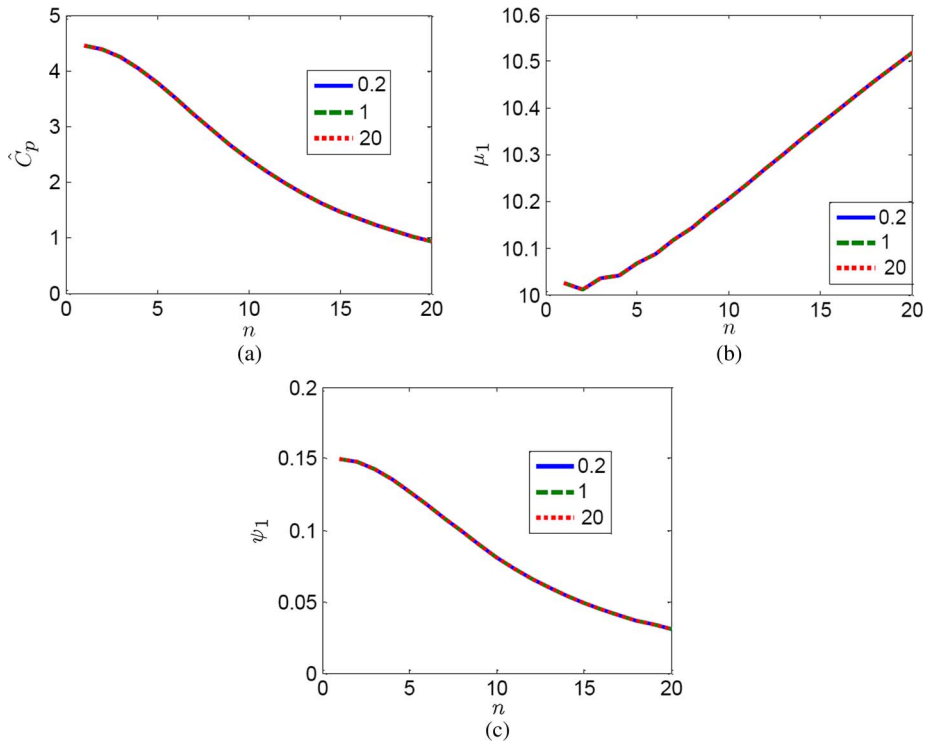

Fig. 19. Relation between the number of members and key power parameters: (a) capacitance, (b) forcing coefficient, and (c) coupling coefficient; the legend shows the size scale.

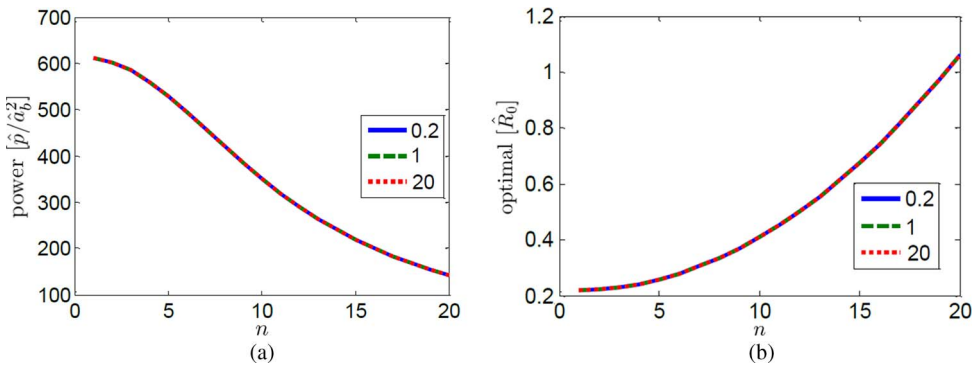

Fig. 20. Relation between the number of members and key power parameters: (a) maximum power transfer function and (b) optimal load resistance; the legend shows the size scale.

key power production parameters $(\widehat{\mu}, \widehat{\psi}, \widehat{C}_p)$ versus number of members. Next, we study how the number of members is related to the dimensionless power. Simultaneously, to test the nondimensionality of our study, we do a scale analysis. We consider three structures: a typical MEMS energy harvester, a harvester from the same materials but where all the dimensions are 1/5 of the original dimensions, and one where all the dimensions are 20 times the original. We check to see if in spite of their different sizes we can model three energy harvesters using the same set of dimensionless parameters.

As shown in Fig. 19, for larger number of members, less dimensionless capacitance, more dimensionless forcing term, and less dimensionless electromechanical coupling result. The decrease in dimensionless capacitance seems at first counter-intuitive since the more members, the more the surface area and capacitance. We must however note that, since the natural frequency decreases, the dimensionless capacitance and not the capacitance itself, decreases with the number of members.

Fig. 20(a) shows that the reduction in the coupling coefficient comes at a price, and the dimensionless power decreases with using more number of members. Comparing Figs. 20(a), 19(c) and 6 reveals that the drop in coupling coefficient and consequently power is due to the decrease in bending/torsion deflection ratio. In other words, the drop is because the vibrations become more and more torsional, and the torsional deflections do not result any charge due to the nature of torsional coupling. The optimal resistance increases with the number of members as shown in Fig. 20(b). In Fig. 19 as well as Fig. 20, the parameters are independent of the scale, which confirms that our analysis is truly dimensionless.

J. Reflections on Zigzag Structure and MEMS Vibrational Harvesting in General

At this point, we can clearly examine the practicality of the zigzag structure. Comparing to other MEMS harvesters, the use of zigzag geometry significantly enhances our tuning capabilities without sacrificing the strength of the device. Referring to Fig. 11, there is a four order of magnitude difference between the power at resonance frequency versus the off resonance power. This implies that the tuning capability can increase the power output by four orders of magnitude provided the other parameters stay the same. The power production variable, however, decreases with the number of members as shown in Fig. 20(a). Fortunately, the tuning capability significantly outperforms the drop, and overall the zigzag structure is proven to be a literally powerful solution for micropower generation. For a case study that showcases the significant power enhancement using the zigzag design, the reader may refer to [15].

The dimensionless analysis [particularly (37)] shows the limits of microscale energy harvesting. We compare a large size vibration harvester with a microscale. The actual power is related to dimensionless as $p = \hat{p}\rho A l^3 \omega_1^3$. The device should always be tuned to the base excitation so ω_1 is fixed. The equivalent density of the bimorph is also constant. According to (36), $\hat{p}$ is proportional to $\hat{a}_b^2$ which in turn is inversely proportional to l^2. The area is proportional to l^2. Thus, the the formula suggests that by shrinking the dimensions by an order of magnitude, the power drops by three orders. In other words, the produced power is to some extent proportional to the volume of the harvester, provided the device is tuned to excitations. This argument suggests selection of power per energy harvester volume as a figure of merit. It also implies that unless necessary, the size of harvesters must not be reduced to microscale since that results in significant reduction of power capacity. The argument is general and does not detract from the practicality of the zigzag approach. The implementation of the meandering geometry is a necessity to tune the frequency and maximize the power production of the MEMS harvesters.

IX. Conclusion

A nondimensional analysis of the novel zigzag beam structure for low-frequency MEMS energy harvesting was presented. It was shown that the natural frequencies of the structure are functions of six dimensionless parameters. The full electromechanical problem was also modeled, and the power output of the device was shown to be a function of 12 dimensionless variables, six of them previously encountered in an examination of the natural frequencies. The vibration and energy harvesting analyses were summarized in the graphs showing the relation between the natural frequency and power output and the dimensionless parameters affecting them. In addition, the bending share in the deflection of the structure and key power production parameters were studied. The variations of power output according to the changes in excitation frequency and shunt resistance were investigated. From that point on, the power output at optimal excitation frequency and across the optimal resistance was investigated. The variations of the optimal power generation with each of the other corresponding dimensionless parameters were examined. The analysis is summarized in an easy to use form, so that the other researchers can utilize our dimensionless study to conveniently design and predict the behavior of zigzag structures of arbitrary dimensions and materials for vibrational power harvesting.

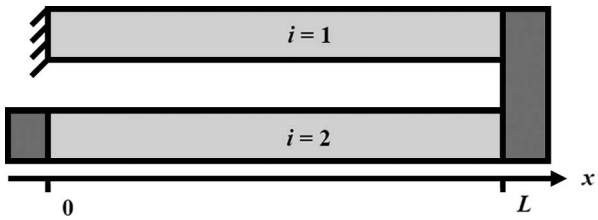

Fig. 21. Schematic diagram of a two member zigzag with tip and link masses.

Appendix
Orthogonality of the Mode Shapes

The mode shapes are extensively used in the electromechanical vibration analysis of the zigzag structure. In this section, we check to see if the derived mode shapes are orthogonal. For briefness of calculations, we consider a two member zigzag (Fig. 21) with both tip and link masses. The proof can be generalized to n member zigzag structure.

We note the nth bending mode shape of the ith member by ${}_i\phi_n$ and the corresponding torsion mode shape by ${}_iB_n$. The free vibration equations (10) and (11) are rewritten in modal form, are premultiplied by the mode shapes, and are integrated over the structure to give

$$\sum_{i=1}^{2}\sum_{n=1}^{\infty}\left(\int_0^L {}_i\phi_m Y I_i \phi_n^{(4)} dx T_n(t) + \int_0^L {}_i\phi_m \rho A_i \phi_n dx \ddot{T}_n(t)\right) = 0 \tag{40}$$

$$\sum_{i=1}^{2}\sum_{n=1}^{\infty}\left(\int_0^L {}_iB_m G J_i B_n^{(2)} dx T_n(t) + \int_0^L {}_iB_m I_{p\,i} B_n dx \ddot{T}_n(t)\right) = 0. \tag{41}$$

We then integrate by parts the first integrals in (40) and (41) and apply the boundary, equilibrium, and continuity conditions in (3)–(6) which result

$$\sum_{n=1}^{\infty}\left\{\left[YI\int_0^L {}_i\phi_m''\,{}_i\phi_n'' dx\right] + dYI_iB_m(L)\,{}_2\phi_n^{(3)}\right\}T_n = -\sum_{n=1}^{\infty}\left\{\sum_{i=1}^{2}\left[\rho A\int_0^L {}_i\phi_{m\,i}\phi_n dx\right] + {}_2\phi_m(0)m_{t\,2}\phi_n(0) + {}_1\phi_m(L)m_{l1}\phi_n(L)\right\}\ddot{T}_n \tag{42}$$

$$\sum_{n=1}^{\infty}\left\{\sum_{i=1}^{2}\left[GJ\int_0^L {}_iB'_n{}_iB'_m dx\right]-dYI\,{}_iB_m(L){}_2\phi_2^{(3)}\right\}T_n$$
$$=-\sum_{n=1}^{\infty}\left\{\sum_{i=1}^{2}\left[I_p\int_0^L {}_iB_m{}_iB_n dx\right]\right\}\bar{T}_n. \tag{43}$$

We then add (42) and (43) to cancel the mixed terms. Since we are considering the free vibrations, we can substitute $\bar{T}_n$ by $-\omega_n^2 T_n$

$$\sum_{i=1}^{2}\left[YI\int_0^L {}_i\phi''_m{}_i\phi''_n dx+GJ\int_0^L {}_iB'_n{}_iB'_m dx\right]T_n(t)$$
$$-\left\{\sum_{i=1}^{2}\left[\rho A\int_0^L {}_i\phi_m{}_i\phi_n dx+I_p\int_0^L {}_iB_m{}_iB_n dx\right]\right.$$
$$\left.+{}_2\phi_m(0)m_t\,{}_2\phi_n(0)+{}_1\phi_m(L)m_l\,{}_1\phi_n(L)\right\}\omega_n^2T_n(t)$$
$$=0. \tag{44}$$

It can be proven [19], [24], [25] that (44) implies that

$$\sum_{i=1}^{2}\left[\rho A\int_0^L {}_i\phi_m{}_i\phi_n dx+I_p\int_o^L {}_iB_m{}_iB_n dx\right]$$
$$+{}_2\phi_m(0)m_t{}_2\phi_n(0)+{}_1\phi_m(L)m_l{}_1\phi_n(L)=a_n\delta_{mn} \tag{45}$$

$$\sum_{i=1}^{2}\left[YI\int_0^L {}_i\phi''_m{}_i\phi''_n dx+GJ\int_0^L {}_iB'_n{}_iB'_m dx\right]=a_n\omega_n^2\delta_{mn}. \tag{46}$$

The parameter a_n represents an arbitrary number.

ACKNOWLEDGMENT

The first author would like to thank Prof. Masoud Agah for his course on MEMS fabrication during which the idea of using the zigzag design occurred to him.

REFERENCES

[1] D. J. Leo, *Engineering Analysis of Smart Material Systems*. Hoboken, NJ: Wiley, 2007.
[2] F. Lu, H. Lee, and S. Lim, "Modeling and analysis of micro piezoelectric power generators for micro-electromechanical-systems applications," *Smart Mater. Struct.*, vol. 13, no. 1, pp. 57–63, Feb. 2004.
[3] Y. Jeon, R. Sood, J. Jeong, and S.-G. Kim, "MEMS power generator with transverse mode thin film PZT," *Sens. Actuators A, Phys.*, vol. 122, no. 1, pp. 16–22, 2005.
[4] I. Kuehne, D. Marinkovic, G. Eckstein, and H. Seidel, "A new approach for MEMS power generation based on a piezoelectric diaphragm," *Sens. Actuators A, Phys.*, vol. 142, no. 1, pp. 292–297, Mar. 2008.
[5] Q. Zheng and Y. Xu, "Asymmetric air-spaced cantilevers for vibration energy harvesting," *Smart Mater. Struct.*, vol. 17, no. 5, p. 055009, Oct. 2008.
[6] N. Sato, K. Ono, T. Shimamura, K. Kuwabara, M. Ugajin, S. Mutoh, H. Morimura, H. Ishii, J. Kodate, and Y. Sato, "Energy harvesting by MEMS vibrational devices with electrets," in *Proc. TRANSDUCERS*, 2009, pp. 513–516.
[7] H.-B. Fang, J.-Q. Liu, Z.-Y. Xu, L. Dong, L. Wang, D. Chen, B.-C Cai, and Y. Liu, "Fabrication and performance of MEMS-based piezoelectric power generator for vibration energy harvesting," *Microelectron. J.*, vol. 37, no. 11, pp. 1280–1284, Nov. 2006.
[8] D. Shen, J.-H. Park, J. Ajitsaria, S.-Y. Choe, H. C. Wikle, III, and D.-J. Kim, "The design, fabrication and evaluation of a MEMS PZT cantilever with an integrated Si proof mass for vibration energy harvesting," *J. Micromech. Microeng.*, vol. 18, no. 5, p. 55 017, May 2008.
[9] J.-Q. Liu, H.-B. Fang, Z.-Y. Xu, X.-H. Mao, X.-C. Shen, D. Chen, H. Liao, and B.-C. Cai, "A MEMS-based piezoelectric power generator array for vibration energy harvesting," *Microelectron. J.*, vol. 39, no. 5, pp. 802–806, May 2008.
[10] J. C. Park, D. H. Lee, J. Y. Park, Y. S. Chang, and Y. P. Lee, "High performance piezoelectric MEMS energy harvester based on D33 mode of PZT thin film on buffer-layer with PBTIO3 inter-layer," in *Proc. TRANSDUCERS*, 2009, pp. 517–520.
[11] R. Elfrink, M. Renaud, T. M. Kamel, C. de Nooijer, M. Jambunathan, M. Goedbloed, D. Hohlfeld, S. Matova, V. Pop, L. Caballero, and R. van Schaijk, "Vacuum-packaged piezoelectric vibration energy harvesters: Damping contributions and autonomy for a wireless sensor system," *J. Micromech. Microeng.*, vol. 20, no. 10, p. 104 001, Oct. 2010.
[12] U. Bartsch, J. Gaspar, and O. Paul, "Low-frequency two-dimensional resonators for vibrational micro energy harvesting," *J. Micromech. Microeng.*, vol. 20, no. 3, p. 035016, Mar. 2010.
[13] B. Yang, C. Lee, R. K. Kotlanka, J. Xie, and S. P. Lim, "A MEMS rotary comb mechanism for harvesting the kinetic energy of planar vibrations," *J. Micromech. Microeng.*, vol. 20, no. 6, p. 065017, Jun. 2010.
[14] M. A. Karami and D. J. Inman, "Analytical modeling and experimental verification of the vibrations of the zigzag micro-structure for energy harvesting," *J. Vib. Acoust.*, vol. 133, no. 1, pp. 011002-1–011002-10, Feb. 2011.
[15] M. A. Karami and D. J. Inman, "Electromechanical modeling of the low frequency zigzag micro energy harvester," *J. Intell. Mater. Syst. Struct.*, vol. 22, no. 3, pp. 271–282, 2011.
[16] H. Hu, H. Xue, and Y. Hu, "A spiral-shaped harvester with an improved harvesting element and an adaptive storage circuit," *IEEE Trans. Ultrason., Ferroelectr., Freq. Control*, vol. 54, no. 6, pp. 1177–1187, Jun. 2007.
[17] M. A. Karami, B. Yardimoglu, and D. J. Inman, "Coupled out of plane vibrations of spiral beams for micro-scale applications," *J. Sound Vib.*, vol. 329, no. 26, pp. 5584–5599, Dec. 2010.
[18] A. Erturk and D. Inman, "Electromechanical modeling of cantilevered piezoelectric energy harvesters for persistent base motions," in *Energy Harvesting Technologies*. New York: Springer-Verlag, 2008.
[19] D. J. Inman, *Engineering Vibration*, 3rd ed. Englewood Cliffs, NJ: Prentice-Hall, 2007.
[20] A. Erturk and D. Inman, "A distributed parameter electromechanical model for cantilevered piezoelectric energy harvesters," *J. Vib. Acoust.*, vol. 130, no. 4, p. 041002, Aug. 2008.
[21] F. White, "Dimensional analysis and similarity," in *Fluid Mechanics*. New York: McGraw-Hill, 1998.
[22] N. Kong, T. Cochran, D. S. Ha, H.-C. Lin, and D. J. Inman, "A self-powered power management circuit for energy harvested by a piezoelectric cantilever," pp. 2154–2160, Feb. 2010.
[23] N. Kong, D. Ha, A. Erturk, and D. J. Inman, "Resistive impedance matching circuit for piezoelectric energy harvesting," *J. Intell. Mater. Syst. Struct.*, vol. 21, pp. 1293–1302, Sep. 2010, 1045389X09357971v1.
[24] L. Meirovitch, *Analytical Methods in Vibration*. New York: Macmillan, 1967.
[25] S. S. Rao, *Vibration of Continuous Systems*. Hoboken, NJ: Wiley, 2007.

M. Amin Karami received the B.Sc. degree in mechanical engineering from Sharif University of Technology, Tehran, Iran, in 2004, the Master of Applied Science degree in mechanical engineering from The University of British Columbia, Vancouver, BC, Canada, in 2006, and the Ph.D. degree in engineering mechanics from Virginia Polytechnic Institute and State University (Virginia Tech), Blacksburg, in 2011.

He is a Postdoctoral Research Fellow in the Department of Aerospace Engineering at the University of Michigan, Ann Arbor. He was a member of the inaugural class of the ICTAS Doctoral Scholars Program and worked in the Center for Intelligent Material Systems and Structures (CIMSS) at Virginia Tech. His research interests include smart materials, energy harvesting, microelectromechanical systems, nonlinear vibrations, and dynamics of nonlinear systems.

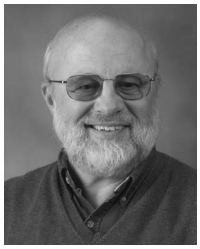

Daniel J. Inman received the Ph.D. degree in mechanical engineering from Michigan State University, East Lansing, in 1980.

He is Chair of the Department of Aerospace Engineering at the University of Michigan, Ann Arbor, as well as the C. L. "Kelly" Johnson Collegiate Professor. Since 1980, he has published eight books (on vibration, energy harvesting, control, statics, and dynamics), eight software manuals, 20 book chapters, over 254 journal papers and 511 proceedings papers, given 50 keynote or plenary lectures, graduated 54 Ph.D. students and supervised more than 75 M.S. degrees. He works in the area of applying smart structures to solve engineering problems including energy harvesting, structural health monitoring, vibration suppression and morphing.

Prof. Inman is a Fellow of the ASME, AIAA, IIAV and AAM.